










## Role of structural defects in mediating disordering processes at irradiated epitaxial Fe<sub>3</sub>O<sub>4</sub>/Cr<sub>2</sub>O<sub>3</sub> interfaces

Tiffany C. Kaspar <sup>1,\*</sup>, Steven R. Spurgeon <sup>2,3</sup>, Kayla H. Yano <sup>2</sup>, Bethany E. Matthews <sup>2</sup>, Mark E. Bowden <sup>1</sup>,  
Colin Ophus <sup>4</sup>, Hyosim Kim <sup>5</sup>, Yongqiang Wang <sup>5</sup>, and Daniel K. Schreiber <sup>2</sup>

<sup>1</sup>Physical and Computational Sciences Directorate, Pacific Northwest National Laboratory, Richland, Washington 99354, USA

<sup>2</sup>Energy and Environment Directorate, Pacific Northwest National Laboratory, Richland, Washington 99354, USA

<sup>3</sup>Department of Physics, University of Washington, Seattle, Washington 98195, USA

<sup>4</sup>NCEM, Molecular Foundry, Lawrence Berkeley National Laboratory, Berkeley, California 94720, USA

<sup>5</sup>Materials Science and Technology Division, Los Alamos National Laboratory, Los Alamos, New Mexico 87545, USA



(Received 30 March 2023; accepted 21 August 2023; published 14 September 2023)

Disordering processes in oxide materials are complicated by the presence of interfaces, which can serve as either point defect sinks or accumulation sites; the response depends on factors such as interfacial structure, chemistry, and termination. We have characterized the disordering of epitaxial Fe<sub>3</sub>O<sub>4</sub>(111)/Cr<sub>2</sub>O<sub>3</sub>(0001) thin film heterostructures after 400 keV Ar<sup>2+</sup> radiation at room temperature. The density of misfit dislocations in both the Fe<sub>3</sub>O<sub>4</sub> overlayer and Cr<sub>2</sub>O<sub>3</sub> buffer layer is varied by changing the thickness of Cr<sub>2</sub>O<sub>3</sub> to be pseudomorphically strained to the Al<sub>2</sub>O<sub>3</sub> (0001) substrate (5 nm thick) or partially relaxed (20 nm thick), as confirmed by Bragg filtering analysis of scanning transmission electron microscopy images. In both cases, irradiation leads to damage accumulation on the Fe<sub>3</sub>O<sub>4</sub> side of the heterointerface, as shown by Rutherford backscattering spectrometry measurements in the channeling geometry. However, the interface with more misfit dislocations exhibits disordering at a faster rate than the less-defective interface. Likewise, layer-resolved electron energy loss spectroscopy reveals interfacial reduction of Fe after irradiation at the more defective interface. Intermixing of Cr across the interface is observed by atom probe tomography, which is likely facilitated by the generation of Cr interstitials in Cr<sub>2</sub>O<sub>3</sub> under irradiation.

DOI: [10.1103/PhysRevMaterials.7.093604](https://doi.org/10.1103/PhysRevMaterials.7.093604)

### I. INTRODUCTION

Understanding the mechanisms of disordering and recovery in crystalline materials is critical to predict their behavior under external stimuli. For example, one initial response of materials to energetic ion irradiation is disordering via the formation of Frenkel pairs as atoms are knocked off their lattice sites. In metals and alloys, these primary knock-on processes are reasonably well understood [1], but the evolution of the resulting nonequilibrium point defect population and its interaction with defects and imperfections can be complex and difficult to predict [2]. Irradiation of oxides introduces additional complications [3–6] including the potentially significant ionizing and thermal effects of inelastic electronic energy loss processes; the different responses of the anion and cation sublattices to both primary knock-on events and inelastic energy loss processes; and the generation, recombination, and/or transport of charged point defects. Therefore, in addition to nonequilibrium point defect and defect cluster populations, in oxides, these processes lead to global electronic and structural changes that are poorly understood.

Interfaces (e.g., grain boundaries, free surfaces, or phase boundaries) in irradiated oxides can serve as defect sinks, providing sites for efficient point defect recombination or,

conversely, defect accumulation sites that result in more significant disordering [7,8]. Heterostructures consisting of epitaxial oxide thin film(s) on a single-crystal substrate can be systematically manipulated to explore the effect of interface structure, chemistry, and termination on disordering processes in a model system where the tailored heterointerface is the dominant (but not the only) defect. We and others have previously studied the effect of interface configuration on radiation response, observing widely varying behavior [9–15]. For example, irradiation of epitaxial SrTiO<sub>3</sub> deposited on LaAlO<sub>3</sub>(001) with 260–400 keV Ne<sup>2+</sup> induced amorphization in LaAlO<sub>3</sub> first followed by amorphization of SrTiO<sub>3</sub>; in both cases, the amorphization started at the interface and proceeded outward [16]. Chemical changes were also observed at the interface in the form of accumulated oxygen on the LaAlO<sub>3</sub> side of the interface. Atomistic simulations suggested that thermodynamic driving forces exist for defect flow across the heterointerface, and these driving forces were speculated to be responsible in part for the oxygen accumulation. In contrast to the behavior of SrTiO<sub>3</sub>/LaAlO<sub>3</sub>, amorphization of irradiated BaTiO<sub>3</sub> on SrTiO<sub>3</sub>(001) proceeded from the film surface and did not progress as far as the heterointerface, although defect agglomerates and dislocation loops were observed in the interfacial region [17]. The heterointerface was also observed to play an important role in the radiation response of anatase TiO<sub>2</sub> deposited on SrTiO<sub>3</sub>(001): A denuded zone was observed on the TiO<sub>2</sub>

\*tiffany.kaspar@pnnl.gov

side of the interface, while SrTiO<sub>3</sub> amorphization proceeded from the interface [18,19]. The different response of TiO<sub>2</sub> vs SrTiO<sub>3</sub> may be related to the ease with which TiO<sub>2</sub> can accommodate nonstoichiometry, particularly oxygen deficiency via the formation of Ti<sup>3+</sup> interstitials. We have also observed more complex percolation of disorder during *in situ* irradiation in the electron microscope, observing the emergence of local regions of disorder that progress toward fully amorphous films in the case of LaMnO<sub>3</sub>/STO [20]. In these studies, structural defects, such as misfit dislocations arising from epitaxial lattice mismatch, were not considered but can serve as nanoscale imperfections that further influence irradiation behavior [7,21,22].

Oxides are one of the primary corrosion products of many nuclear structural materials in service conditions [23]. In contact with aqueous coolants, these corrosion products develop into complex duplex layers of Fe-rich (outer) and Cr-rich (inner) oxides [24]. To understand how these layers develop in the early stages of oxidation, a model Fe-Cr-Ni steel alloy was oxidized by *in situ* O<sub>2</sub>, resulting in a layered structure of Fe<sub>3</sub>O<sub>4</sub>/Cr<sub>2</sub>O<sub>3</sub>/Ni/base alloy observed by atom probe tomography (APT) [25]. Understanding the response of oxide corrosion products to irradiation is of practical importance to predict corrosion rates over service lifetimes, improve material design, and establish component inspection schedules. The irradiation response of the iron oxides prevalent in corrosion products is particularly complex, and therefore, the iron oxides provide a rich system to study structural and stoichiometric changes upon irradiation. Irradiation of nanoparticle films composed of a metallic Fe core and magnetite, Fe<sub>3</sub>O<sub>4</sub>, shell with 5.5 MeV Si<sup>2+</sup> ions was found to result in reduction to wüstite, Fe<sub>1-x</sub>O, due to oxygen loss [26], but irradiation of Fe/Fe<sub>3</sub>O<sub>4</sub> with 1 MeV Ar<sup>+</sup> resulted in oxidation of the metallic Fe layer while appearing to preserve the stoichiometry and crystallinity of the Fe<sub>3</sub>O<sub>4</sub> layer [27]. A nanoscale study of the irradiation of Fe/Fe<sub>3</sub>O<sub>4</sub> with 1 MeV Kr<sup>2+</sup> revealed, via observation by *in situ* transmission electron microscopy (TEM), that defect mobility in Fe<sub>3</sub>O<sub>4</sub> was unexpectedly high, surpassing that of defects in Fe metal [28]. A deeper understanding of defect mechanisms underpinning the stoichiometry and oxidation state changes of the iron oxides under irradiation is necessary to predict their behavior in real-world environments.

In this paper, the radiation response of the Fe<sub>3</sub>O<sub>4</sub>/Cr<sub>2</sub>O<sub>3</sub> interface is studied in a model epitaxial thin film heterostructure. We vary the misfit dislocation density in the epitaxial Fe<sub>3</sub>O<sub>4</sub> and Cr<sub>2</sub>O<sub>3</sub> thin films via control of Cr<sub>2</sub>O<sub>3</sub> buffer layer thickness relative to the critical thickness for epitaxial strain relaxation on Al<sub>2</sub>O<sub>3</sub>(0001) substrates. These heterostructures are then irradiated to a low fluence with 400 keV Ar<sup>2+</sup>. Lattice-scale structural disorder, nanoscale crystallinity, and spatially resolved electronic structure of the irradiated Fe<sub>3</sub>O<sub>4</sub> are correlated to gain insights into the mechanism of initial disordering processes and reveal the role of interfaces and crystalline defects on damage accumulation.

## II. METHODS

Epitaxial Cr<sub>2</sub><sup>18</sup>O<sub>3</sub> films were deposited on Al<sub>2</sub>O<sub>3</sub>(0001) substrates by oxygen-plasma-assisted molecular beam epi-

taxy (OPA-MBE) as described previously [29]. Briefly, Al<sub>2</sub>O<sub>3</sub>(0001) substrates were heated to the deposition temperature of 730 °C while maintaining a flow of activated oxygen through the electron cyclotron resonance (ECR) microwave plasma source at an oxygen pressure of  $2 \times 10^{-5}$  Torr. The gas source was then switched from natural abundance (NA) O<sub>2</sub> (>99.7% <sup>16</sup>O<sub>2</sub>) to 99% enriched <sup>18</sup>O<sub>2</sub> by reducing the NA O<sub>2</sub> gas flow through the plasma until the chamber pressure reached  $\sim 1 \times 10^{-5}$  Torr, then introducing the <sup>18</sup>O<sub>2</sub> gas flow to bring the chamber pressure back to  $2 \times 10^{-5}$  Torr as the NA O<sub>2</sub> flow was reduced to zero. The flow of <sup>18</sup>O<sub>2</sub> through the plasma was allowed to equilibrate for 3 min before deposition began. NA Cr was evaporated from an electron beam evaporator at a deposition rate of 0.1 Å Cr<sub>2</sub><sup>18</sup>O<sub>3</sub> s<sup>-1</sup> to a final film thickness of 5 or 20 nm. The same gas handling procedure was then followed to switch back to NA O<sub>2</sub> for the deposition of NA Fe<sub>3</sub>O<sub>4</sub>. While maintaining the deposition temperature of 730 °C, the ECR plasma was turned off, and the oxygen partial pressure was reduced to  $1 \times 10^{-5}$  Torr in preparation for the deposition of Fe<sub>3</sub>O<sub>4</sub>. NA Fe was evaporated from an electron beam evaporator at a deposition rate of 0.24 Å Fe<sub>3</sub>O<sub>4</sub> s<sup>-1</sup> to a final film thickness of 30 nm. The depositions were monitored with reflection high-energy electron diffraction (RHEED). At the end of the deposition, the Fe<sub>3</sub>O<sub>4</sub>/Cr<sub>2</sub>O<sub>3</sub> heterostructures were cooled in vacuum. Epitaxial orientation and strain state of the films were measured *ex situ* using x-ray diffraction (XRD) collected using a Rigaku SmartLab diffractometer with a rotating Cu anode operated at 45 kV and 200 mA. The incident beam (Cu K $\alpha$ ) was filtered using a two-bounce Ge(220) monochromator, and a matching monochromator was employed for the diffracted beam.

Areas of  $\sim 5 \times 2.5$  mm<sup>2</sup> of the as-grown films were irradiated at Los Alamos National Laboratory in the Ion Beam Materials Lab with 400 keV Ar<sup>2+</sup> at room temperature in vacuum to a fluences of  $2.8 \times 10^{14}$  and  $1.4 \times 10^{15}$  ions cm<sup>-2</sup>. SRIM simulations [30] using full cascade mode (displacement energies of 40 eV for Fe and Cr, 28 eV for O, and 27 eV for Al) indicated that the displacements per atom (dpa) at a depth of 30 nm (at the Fe<sub>3</sub>O<sub>4</sub>/Cr<sub>2</sub>O<sub>3</sub> interface) were 0.1 and 0.5 dpa, respectively, for the two fluences. Rutherford backscattering spectrometry (RBS) data were then collected from both as-grown and irradiated regions of each film using 2.3 MeV He<sup>+</sup> from a 3 MV Pelletron accelerator. The backscattering Si detector was located at 165° in reference to the incident beam in the IBM geometry [31], and channeling data were collected along the [0001] direction of the corundum structure (Al<sub>2</sub>O<sub>3</sub>, Cr<sub>2</sub>O<sub>3</sub>) and, equivalently, the [111] direction of the spinel structure of Fe<sub>3</sub>O<sub>4</sub>.

Cross-sectional scanning TEM (STEM) samples were prepared using a FEI Helios NanoLab DualBeam Ga<sup>+</sup> focused ion beam (FIB) microscope with a standard lift-out procedure. STEM images were acquired on a probe-corrected Thermo Fisher Themis Z microscope operating at 300 kV, with a convergence semiangle of 25.2 mrad and an approximate collection angle range of 65–200, 16–62, and 8–14 mrad for high-angle annular dark field (STEM-HAADF), medium-angle annular dark field (STEM-MAADF), and low-angle annular dark field (STEM-LAADF), respectively. STEM energy-dispersive x-ray spectroscopy (STEM-EDS) composition maps were acquired using a SuperX detector. Electron

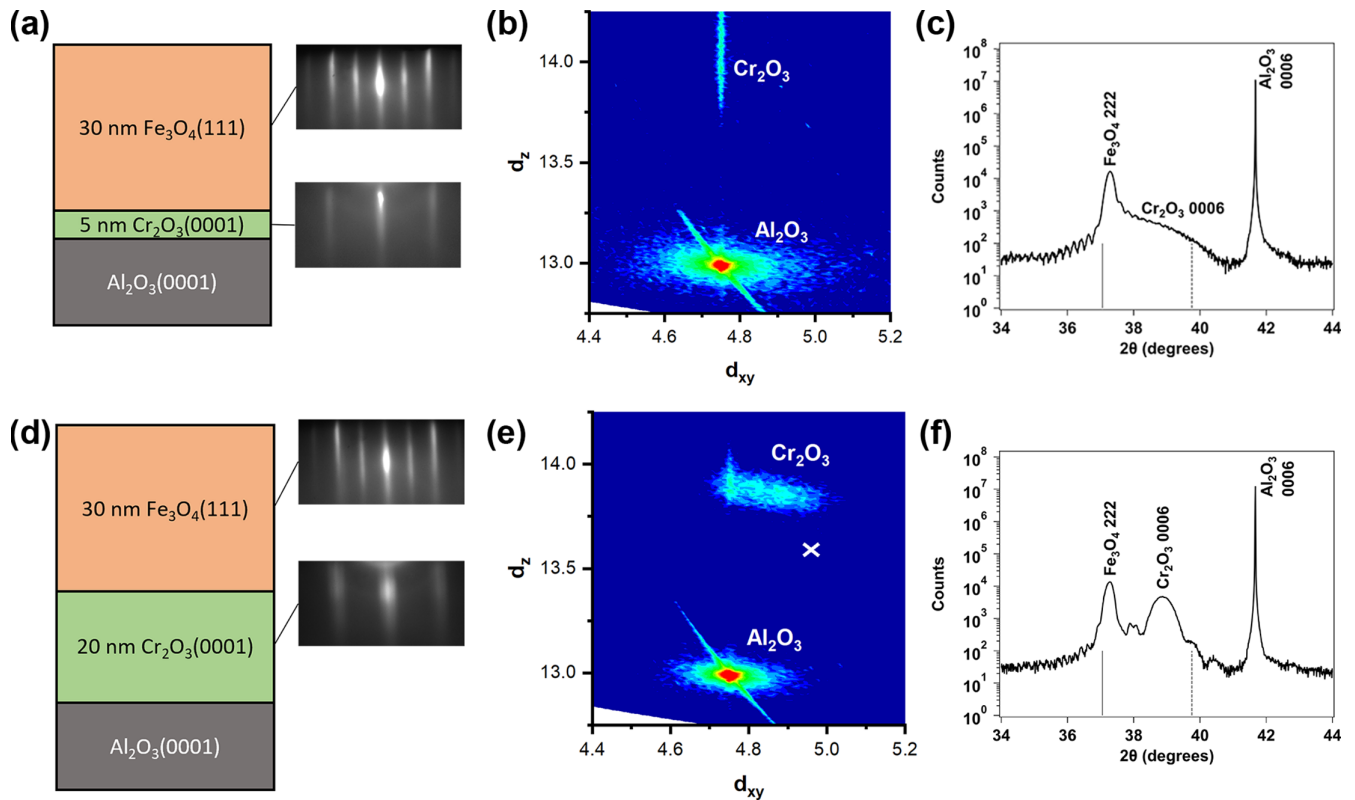


FIG. 1. Heterostructure schematic and reflection high-energy electron diffraction (RHEED) patterns captured after deposition of  $\text{Cr}_2\text{O}_3$  (at growth temperature) and deposition of  $\text{Fe}_3\text{O}_4$  (after cooling to room temperature) for (a) 5 nm and (d) 20 nm  $\text{Cr}_2\text{O}_3$  buffer layers. X-ray diffraction (XRD) direct space maps of the  $\text{Al}_2\text{O}_3$  and  $\text{Cr}_2\text{O}_3$  [1010] direction for (b) thin and (e) thick  $\text{Cr}_2\text{O}_3$  buffer layers. White cross in (e) indicates the  $d$  spacings of relaxed  $\text{Cr}_2\text{O}_3$ . Out-of-plane XRD patterns for (c) 30 nm  $\text{Fe}_3\text{O}_4$ /5 nm  $\text{Cr}_2\text{O}_3$ / $\text{Al}_2\text{O}_3$  (0001) and (f) 30 nm  $\text{Fe}_3\text{O}_4$ /20 nm  $\text{Cr}_2\text{O}_3$ / $\text{Al}_2\text{O}_3$  (0001). Positions for the bulk  $\text{Fe}_3\text{O}_4$  (222) and  $\text{Cr}_2\text{O}_3$  (0006) reflections are indicated by solid and dashed lines, respectively.

energy loss spectroscopy (STEM-EELS) measurements were performed with a GIF Continuum Spectrometer using the DualEELS mode, a  $0.3 \text{ eV ch}^{-1}$  dispersion, and a  $130\times$  binning in the nondispersive direction. Data were subsequently corrected for energy drift, and a power-law background correction was applied prior to each edge of interest for final analysis. The STEM-HAADF images of crystalline lattices were analyzed using Bragg filtering analysis methods, including geometric phase analysis [32], implemented in custom MATLAB scripts. First, we computed the image Fourier transform, then defined a two-dimensional (2D) Gaussian mask with a standard deviation equal to 0.003 Nyquist units that spanned the Bragg peaks of interest from the film and/or substrate. From the inverse Fourier transform of the masked image, we computed the phase (after removing the carrier wave) to identify misfit dislocations at the film-substrate interface from spiral phase singularities and used the real value of the filtered images to find the positions of the lattice planes.

APT specimens were prepared using both a FEI Helios NanoLab DualBeam  $\text{Ga}^+$  FIB and a FEI Quanta 3D FEG FIB according to established procedures [33]. Specimens were analyzed with a CAMECA LEAP 4000X HR at a base temperature of 40 K and a pressure of  $<2.7 \times 10^{-9}$  Pa. Laser-assisted field evaporation ( $\lambda = 355 \text{ nm}$ ) was used to analyze the samples at a pulse rate of 250 kHz and a pulse energy of 60 pJ. Detection rates were kept at 0.003 detected ions per pulse by varying the applied voltage. All data were

reconstructed using the CAMECA Integrated Visualization and Analysis Software (IVAS 3.8.8). Films were grown epitaxially on  $\text{Al}_2\text{O}_3$ (0001) substrates, allowing for the (0001) and (111) poles of the  $\text{Cr}_2\text{O}_3$  and  $\text{Fe}_3\text{O}_4$ , respectively, to be captured. Reconstructions were made using the bilayer-to-bilayer spacing of the  $\text{Cr}_2\text{O}_3$  ( $2.3 \text{ \AA}$ ) and  $\text{Fe}_3\text{O}_4$  (every other layer at  $4.8 \text{ \AA}$ ) when available. We discuss the resolution limits of this method elsewhere [34].  $\text{Cr}_2\text{O}_3$  spacing was more challenging to resolve in the 5-nm-thick film. Representative mass spectra, bilayer spacings, and  $^{18}\text{O}$  enrichment are provided in the Supplemental Material [35].

### III. RESULTS

#### A. Structure of as-grown films

The epitaxial deposition of isostructural  $\text{Cr}_2\text{O}_3$ (0001) ( $a = 4.97 \text{ \AA}$ ) on  $\text{Al}_2\text{O}_3$ (0001) ( $a = 4.76 \text{ \AA}$ ) is well established [36]. The bulk lattice mismatch is  $\delta = (a_{\text{Cr}_2\text{O}_3} - a_{\text{Al}_2\text{O}_3})/a_{\text{Al}_2\text{O}_3} \times 100\% = 4.4\%$ . Chambers *et al.* [37] reported on the deposition of  $\text{Cr}_2\text{O}_3$  on  $\text{Al}_2\text{O}_3$ (0001) by OPA-MBE and showed that, based on analysis of RHEED streak spacing,  $\text{Cr}_2\text{O}_3$  initially grows pseudomorphically on  $\text{Al}_2\text{O}_3$ (0001) but begins to relax as the thickness increases. The critical thickness for  $\text{Cr}_2\text{O}_3$  to relax to nearly the bulk lattice parameters was found to be  $<\sim 12 \text{ nm}$ . As shown in Figs. 1(a)–1(c), the deposition of 5 nm  $\text{Cr}_2\text{O}_3$  on  $\text{Al}_2\text{O}_3$ (0001) by OPA-MBE results in a pseudomorphically strained film, with in-plane

lattice parameters equivalent to those of  $\text{Al}_2\text{O}_3$ . However, deposition of 20 nm of  $\text{Cr}_2\text{O}_3$  under the same conditions [Figs. 1(d)–1(f)] results in a partially relaxed film, with in-plane lattice parameters that have fully relaxed to the bulk values in some regions of film. The existence of residual strain in the film is indicated by both the range of in-plane lattice spacings detected and the out-of-plane (OOP) lattice parameter, which remains considerably larger than the relaxed value [ $c_{\text{Cr}_2\text{O}_3} = 13.59 \text{ \AA}$  compared with  $c_{\text{measured}} \approx 13.9 \text{ \AA}$  in Fig. 1(e)]. Analysis of the RHEED streak spacing on images collected after the deposition of  $\text{Cr}_2\text{O}_3$  confirm that the spacing is  $\sim 2.5\%$  larger after deposition of 20 nm than after deposition of 5 nm of  $\text{Cr}_2\text{O}_3$  (provided in the Supplemental Material [35]). This means that the in-plane lattice parameters at the film surface have relaxed by 2.5% toward the bulk values. Although this is less than the 4.4% expected if the thicker  $\text{Cr}_2\text{O}_3$  film had fully relaxed, it indicates that the lattice mismatch between the thicker, partially relaxed  $\text{Cr}_2\text{O}_3$  buffer layer and the subsequent  $\text{Fe}_3\text{O}_4$  film will be less than that between the thinner, pseudomorphically strained  $\text{Cr}_2\text{O}_3$  buffer layer and  $\text{Fe}_3\text{O}_4$ .

The in-plane spacing on the  $\text{Fe}_3\text{O}_4(111)$  surface is  $d = 5.14 \text{ \AA}$ , and therefore, deposition of  $\text{Fe}_3\text{O}_4(111)$  on  $\text{Cr}_2\text{O}_3(0001)$  will result in compressive in-plane strain in the  $\text{Fe}_3\text{O}_4$  film with a lattice mismatch (assuming bulk lattice parameters for both) of  $\delta = 3.46\%$ . This mismatch increases to  $\delta = 8.03\%$  if the  $\text{Cr}_2\text{O}_3$  is fully pseudomorphically strained to the  $\text{Al}_2\text{O}_3$  substrate. Deposition of  $\text{Fe}_3\text{O}_4(111)$  on the pseudomorphically strained 5 nm  $\text{Cr}_2\text{O}_3$  buffer layer shown in Figs. 1(a)–1(c) is expected to result in a mismatch close to 8.03%, whereas deposition on partially relaxed 20 nm  $\text{Cr}_2\text{O}_3$  [Figs. 1(d)–1(f)] likely results in a lower mismatch (but not as low as the predicted 3.46%). As shown in the OOP XRD patterns in Figs. 1(c) and 1(f), 30 nm  $\text{Fe}_3\text{O}_4$  films on both thicknesses of buffer layer are (111) oriented and exhibit finite-thickness fringes indicative of well-crystallized films with smooth surfaces and interfaces. The OOP lattice parameter of both films is nearly identical at  $d_{(222)} = \sim 2.41 \text{ \AA}$ , which is slightly smaller than the bulk value of  $d_{(222)} = 2.424 \text{ \AA}$ . In-plane tensile strain that would lead to this OOP lattice compression is not expected to occur for deposition on  $\text{Cr}_2\text{O}_3(0001)$ . Instead, the compressed OOP lattice parameter may indicate that the  $\text{Fe}_3\text{O}_4$  films are fully relaxed and somewhat overoxidized, forming a magnetite/maghemite ( $\gamma\text{-Fe}_2\text{O}_3$ ) solid solution [38].

Figures 2(a) and 2(b) present RBS data collected in random (off-normal) and channeling (aligned along  $\text{Fe}_3\text{O}_4[111]/\text{Cr}_2\text{O}_3[0001]$  film normal direction) geometries for both  $\text{Fe}_3\text{O}_4/\text{Cr}_2\text{O}_3$  heterostructures. The backscattering signal from Fe in the  $\text{Fe}_3\text{O}_4$  film is reasonably well separated from that of Cr in the  $\text{Cr}_2\text{O}_3$  buffer layer, allowing them to be analyzed separately. In the channeling geometry, a lower backscattering intensity corresponds to increased crystalline order (such as a lower extent of mosaic spread and/or a lower concentration of defect structures such as dislocations) [39]. In Figs. 2(a) and 2(b), the backscattering signal from Fe appears as two peaks. The higher-channel peak originates from backscattering from the film surface, while the lower-channel peak arises from Fe backscattering at the interface with  $\text{Cr}_2\text{O}_3$ . The lower backscatter signal between

the two peaks represents the bulk of the  $\text{Fe}_3\text{O}_4$  film. Given the depth resolution of RBS, the surface, bulk, and interface regions of the  $\text{Fe}_3\text{O}_4$  film are each  $\sim \frac{1}{3}$  of the total film thickness. The minimum yield  $\chi_{\text{min}}$  is used to quantify the degree of crystalline order in the  $\text{Fe}_3\text{O}_4$  overlayer and the  $\text{Cr}_2\text{O}_3$  buffer layer. Taking the intensity ( $I$ ) at the centroid of the Fe backscatter peak in the random direction and the same position in the channeling direction, the minimum yield is  $\chi_{\text{min}} = I_{\text{channeling}}/I_{\text{random}} = 11.2\%$  for  $\text{Fe}_3\text{O}_4$  deposited on 5 nm  $\text{Cr}_2\text{O}_3$  and  $\chi_{\text{min}} = 12.3\%$  for  $\text{Fe}_3\text{O}_4$  deposited on 20 nm  $\text{Cr}_2\text{O}_3$ . These values compare favorably with previous RBS/channeling measurements of epitaxial  $\text{Fe}_3\text{O}_4$  films deposited on  $\text{MgO}(001)$  [27]. The minimum yields for Cr in the  $\text{Cr}_2\text{O}_3$  buffer layers are significantly worse:  $\chi_{\text{min}} = 65.5\%$  for 5 nm  $\text{Cr}_2\text{O}_3$  and 34.6% for 20 nm  $\text{Cr}_2\text{O}_3$ .

### B. Crystalline disordering with irradiation

After irradiation with 400 keV  $\text{Ar}^{2+}$ , the random backscattering yield for Fe does not change (provided in the Supplemental Material [35]), indicating that no appreciable sputtering occurred at the low doses employed here. However, an increase in disorder is observed in the channeling yields for both Fe and Cr after irradiation. As shown in Fig. 2(c), the channeling yield of Fe remains nearly constant at the  $\text{Fe}_3\text{O}_4$  surface but increases with increasing dose near the interface with  $\text{Cr}_2\text{O}_3$ . Notably, the increase in channeling yield at the interface is fairly linear with dose but exhibits a larger slope for the  $\text{Fe}_3\text{O}_4/5 \text{ nm } \text{Cr}_2\text{O}_3$  heterostructure than for the  $\text{Fe}_3\text{O}_4/20 \text{ nm } \text{Cr}_2\text{O}_3$  stack. The channeling yield of Cr in the  $\text{Cr}_2\text{O}_3$  buffer layers [Fig. 2(d)] increases significantly after a dose of 0.1 dpa. For the 5 nm  $\text{Cr}_2\text{O}_3$  buffer layer, the 0.1 dpa channeling yield increases to the random value. For the 20 nm  $\text{Cr}_2\text{O}_3$  buffer layer, increasing the dose to 0.5 dpa further increases the channeling yield, maintaining a nearly linear relationship of yield with dose.

### C. Local microstructural evolution with irradiation

To further evaluate initial film quality and the evolution of local microstructure with irradiation, we have conducted detailed STEM analysis. Figure 3 and the Supplemental Material [35] show cross-sectional STEM-HAADF images of the as-grown samples. For both buffer thicknesses, we observe fully crystalline as-grown films with nominally expected layer thicknesses. Bragg-filtering analysis of the STEM-HAADF images [40–42] shows the presence of misfit dislocations in the  $\text{Cr}_2\text{O}_3$  and  $\text{Fe}_3\text{O}_4$  films. Bragg-filtering analysis of the  $\text{Cr}_2\text{O}_3$  buffer layers, shown in Figs. 3(b) and 3(d), indicates significant differences in the starting quantity of misfit dislocations, as expected from the target film thicknesses (greater than and less than the critical thickness for epitaxial strain relaxation). Specifically, we observe a low density of structural defects in the 5 nm  $\text{Cr}_2\text{O}_3$  layer [Figs. 3(a) and 3(b)], as reflected in the continuous uniform stripes in Fig. 3(b) in the lower half of the image corresponding to the  $\text{Cr}_2\text{O}_3$  layer, confirming that this film is pseudomorphically strained to the  $\text{Al}_2\text{O}_3$  substrate and few misfit dislocations have formed. In contrast, numerous misfit dislocations are found at the  $\text{Cr}_2\text{O}_3/\text{Al}_2\text{O}_3$  interface for the 20 nm  $\text{Cr}_2\text{O}_3$  layer (Figs. 3(c)

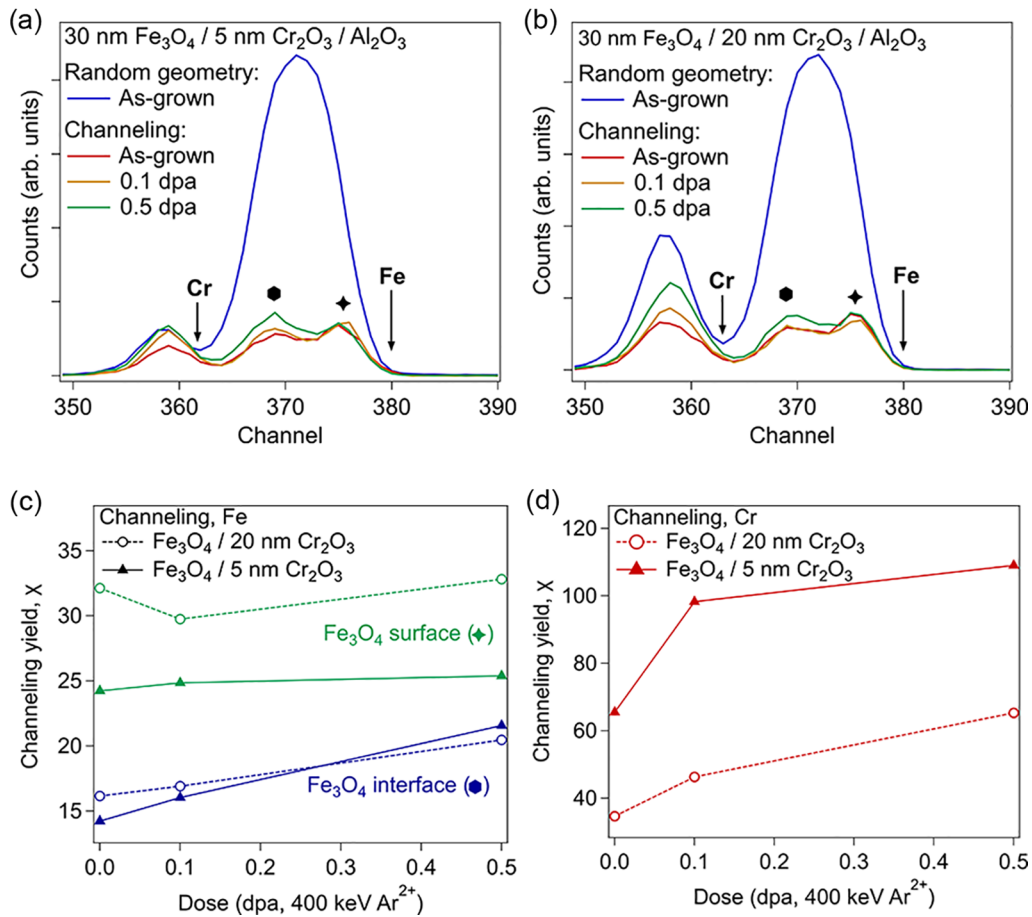


FIG. 2. 2.3 MeV He<sup>+</sup> Rutherford backscattering spectrometry (RBS) spectra of Fe<sub>3</sub>O<sub>4</sub>/Cr<sub>2</sub>O<sub>3</sub>/Al<sub>2</sub>O<sub>3</sub>(0001) thin film heterostructures with (a) 5 nm Cr<sub>2</sub>O<sub>3</sub> and (b) 20 nm Cr<sub>2</sub>O<sub>3</sub> buffer layers. Data are collected in both the random geometry and channeling along the [0001]<sub>corundum</sub>/[001]<sub>spinel</sub> direction. Symbols indicate surface (cross) and interface (hexagon) regions of Fe backscattering. Channeling yield of (c) Fe at the Fe<sub>3</sub>O<sub>4</sub> surface and interface, and (d) Cr in the Cr<sub>2</sub>O<sub>3</sub> buffer layer, for heterostructures with 5 nm (solid) and 20 nm (dashed) Cr<sub>2</sub>O<sub>3</sub> layers.

and 3(d), see also the Supplemental Material [35]) as indicated by the spiral phase singularities [broken stripes in the Cr<sub>2</sub>O<sub>3</sub> region of Fig. 3(d)]. This is expected for a film that has exceeded the critical thickness and has partially relaxed. Likewise, we observe a high density of dislocations in Fe<sub>3</sub>O<sub>4</sub> at the Fe<sub>3</sub>O<sub>4</sub>/Cr<sub>2</sub>O<sub>3</sub> interface on the 5 nm buffered heterostructure [each marked by T in Fig. 3(b)], which is expected given the larger lattice mismatch between Fe<sub>3</sub>O<sub>4</sub> and the pseudomorphically strained Cr<sub>2</sub>O<sub>3</sub> buffer layer. We observe 23 misfit dislocations within this field of view ( $\sim 71 \times \sim 53$  nm) as well as an apparent antiphase boundary [indicated by the arrow in Fig. 3(b)] running through the Fe<sub>3</sub>O<sub>4</sub> layer from the film-substrate interface. It is not possible to determine the integrated dislocation length per unit volume of the film based on the analysis of this single cross-sectional image, but the total dislocation density is assumed to be proportional to the number of observed dislocations.

In contrast, the Fe<sub>3</sub>O<sub>4</sub>/Cr<sub>2</sub>O<sub>3</sub> interface on the 20 nm buffered heterostructure [Fig. 3(d)] exhibits just 16 misfit dislocations in a similar field of view ( $\sim 71 \times \sim 61$  nm). This is approximately a 30% reduction in dislocation density compared with the Fe<sub>3</sub>O<sub>4</sub> film on the thinner Cr<sub>2</sub>O<sub>3</sub> buffer layer. A lower density of misfit dislocations is expected given

the smaller lattice mismatch of Fe<sub>3</sub>O<sub>4</sub> with partially relaxed Cr<sub>2</sub>O<sub>3</sub> in this case.

After irradiation, both heterostructures exhibit more disorder at the Fe<sub>3</sub>O<sub>4</sub>/Cr<sub>2</sub>O<sub>3</sub> interface and more extensive defects in the Fe<sub>3</sub>O<sub>4</sub> layer, as shown by the high-resolution STEM-HAADF images before and after irradiation in Fig. 4 and in the Supplemental Material [35]. The irradiated 20 nm buffered heterostructure [Fig. 4(d)] shows less disorder at the Fe<sub>3</sub>O<sub>4</sub>/Cr<sub>2</sub>O<sub>3</sub> interface than the heterostructure with 5 nm Cr<sub>2</sub>O<sub>3</sub> [Fig. 4(b)], despite the presence of preexisting extended defects running from the film-substrate interface into the Fe<sub>3</sub>O<sub>4</sub>. The fast Fourier transforms (FFTs) in Fig. 4 show increasing diffuse scattering after irradiation. Although surface contamination may contribute to diffuse scattering in the FFT, there is no reason to suspect that the level of contamination would be higher for the irradiated samples since they were prepared using the same approach as for the unirradiated samples. FFTs collected from selected areas that avoid visible extended defects are still found to exhibit diffuse scattering rings. Therefore, the increased diffuse scattering is indicative of underlying lattice disorder, which is commensurate with the lattice disorder observed in the RBS channeling measurements [Figs. 2(a) and 2(b)].

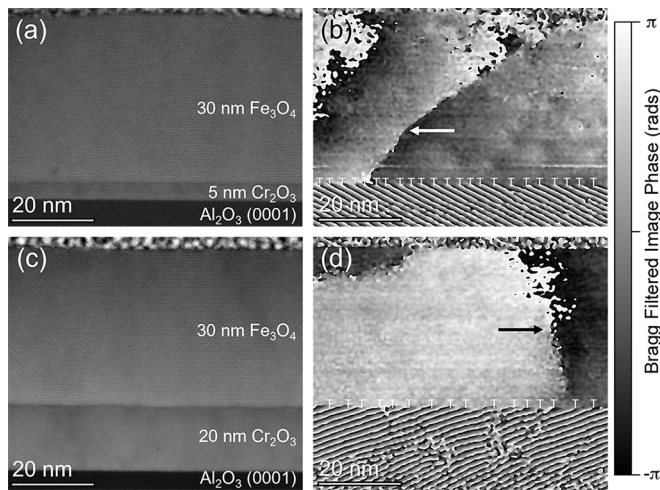


FIG. 3. Scanning transmission electron microscopy (STEM)-high-angle annular dark field (HAADF) images of the as-grown  $\text{Fe}_3\text{O}_4/\text{Cr}_2\text{O}_3$  heterostructures along the  $\text{Fe}_3\text{O}_4$  [110] zone axis with (a) 5 nm and (c) 20 nm  $\text{Cr}_2\text{O}_3$  layers. Bragg filtering analysis (see Supplemental Material [35]) reveals dislocations (marked T's) in the  $\text{Fe}_3\text{O}_4$  layers for (b) 5 nm and (d) 20 nm  $\text{Cr}_2\text{O}_3$  layers. The intensity scale in (b) and (d) covers the range of  $2\pi$  radians ( $360^\circ$ ). Arrows in (b) and (d) indicating apparent antiphase boundaries, indicated by  $\pi$  ( $180^\circ$ ) phase discontinuities, running from the film-substrate interface into the bulk.

To determine whether radiation-enhanced intermixing occurred at the  $\text{Fe}_3\text{O}_4/\text{Cr}_2\text{O}_3$  interfaces, we conducted both STEM-EDS (shown in the Supplemental Material [35]) and STEM-EELS compositional mapping (Fig. 5) of the cation distribution before and after irradiation. Using both techniques, we observe increases in cation interface widths after irradiation. Because of the proximity of the O  $K$  and Cr  $L$  edges in the EELS composition maps, a model-based background fitting approach was used. Integrated signals were computed for each edge, and then the spectra were normalized to the maxima of each signal for the line profiles. We note that, although signal delocalization in EELS can increase the apparent interfacial width [43], we would expect the magnitude of this delocalization to be similar for all four measured samples. As shown in Fig. 5, the interface widths for both Cr and Fe at the interface before irradiation are similar at  $\sim 1.3 \pm 0.1$  nm, as determined by fitting each profile to a sigmoidal function to minimize artifacts arising from the noise in the data; the interface width is then defined as the distance between 90 and 10% of the full intensity of the fitted curve. After irradiation to 0.5 dpa, the Fe interfacial width increases to  $\sim 1.8$ – $1.9$  nm, whereas the Cr interfacial width increases more significantly to  $\sim 2.3$ – $2.4$  nm. In all cases, the interfacial intermixing profiles appear to be largely symmetrical.

To evaluate chemical state changes associated with radiation damage, layer-resolved STEM-EELS spectra were collected near the  $\text{Fe}_3\text{O}_4/\text{Cr}_2\text{O}_3$  interface for both buffer layer thicknesses before and after irradiation, as shown in Fig. 6. At the Fe  $L$  edge, the  $L_3$  peak exhibits a shift to lower energy after irradiation, at both the  $\text{Fe}_3\text{O}_4/\text{Cr}_2\text{O}_3$  interface and 3–4 unit cells into the  $\text{Fe}_3\text{O}_4$  film, for the  $\text{Fe}_3\text{O}_4$  film deposited on the 5 nm  $\text{Cr}_2\text{O}_3$  buffer layer [Fig. 6(a)]. This shift to lower

energy indicates a reduction in average Fe valence. In contrast, the  $\text{Fe}_3\text{O}_4$  film on the 20 nm  $\text{Cr}_2\text{O}_3$  buffer layer exhibits no shift after irradiation [Fig. 6(b)]. Similar evidence of reduction in the  $\text{Fe}_3\text{O}_4$  film deposited on the 5 nm buffer layer is seen in the O  $K$ -edge spectra in Fig. 6(c). In the iron oxides, the O  $K$ -edge EELS spectra consists of a prepeak at  $\sim 530$  eV and a primary peak at  $\sim 539$  eV. The valley between the pre-edge peak and the primary peak is most well defined (i.e., the deepest) for iron oxides that consist entirely of  $\text{Fe}^{3+}$  and becomes less well defined with a lower intensity ratio of the pre-edge peak to the primary peak, as the proportion of  $\text{Fe}^{2+}$  increases [44,45]. Adapting the method described by Varela *et al.* [46], we integrated the measured (not fitted) O  $K$ -edge pre- and main-peak signals for each spectrum and calculated their ratio, as shown in the Supplemental Material [35]. We observe that this ratio decreases upon irradiation for the  $\text{Fe}_3\text{O}_4$  film on the 5 nm  $\text{Cr}_2\text{O}_3$  buffer layer, whereas it does not for the  $\text{Fe}_3\text{O}_4$  film on the 20 nm  $\text{Cr}_2\text{O}_3$  buffer layer. This behavior indicates an overall reduction in the average Fe valence after irradiation for the former that is consistent with the shift of the Fe  $L$  edge to lower energy. Since the analysis of the O  $K$ -edge features can depend on the exact position of the integration window, we emphasize that the peak area ratios must be considered in concert with the behavior of the Fe  $L$ -edge spectra.

APT reconstructions across the heterointerface provide a high spatial resolution measurement of intermixing due to irradiation. As shown in Fig. 7, line profiles taken from one-dimensional (1D) proxigrams of the as-grown heterostructures with 5 and 20 nm  $\text{Cr}_2\text{O}_3$  buffer layers show narrow interface widths with a low level of intermixing for both the anion and cation sublattices. The interface width is quantified as described above for the STEM-EELS profiles: first fitting each profile to a sigmoidal function to minimize artifacts arising from the noise in the data; the interface width is then defined as the distance between 90 and 10% of the full intensity of the fitted curve. At the  $\text{Cr}_2^{18}\text{O}_3/\text{Fe}_3\text{O}_4$  interface, the interfacial width of the oxygen sublattice [defining the isotopic fraction of  $^{18}\text{O}$  as  $f_{^{18}\text{O}} = N_{^{18}\text{O}}/(N_{^{18}\text{O}} + N_{^{16}\text{O}})$ , where  $N$  is the number of  $\text{O}^{1+}$  ions] is on the order of  $\sim 0.5$ – $1.5$  nm for both as-grown samples, as shown by the dark shading in Fig. 7. The interfacial width on the cation sublattice for both as-grown heterostructures is  $\sim 1.5$ – $2$  nm for Cr and  $\sim 1$  nm for Fe. After irradiation to 0.5 dpa, intermixing increases, as suggested by the STEM-EDS results above. On the anion sublattice, the extent of intermixing of  $^{18}\text{O}$  and  $^{16}\text{O}$  depends on the buffer layer thickness: The interfacial width increases to  $\sim 5$  nm for the  $\text{Fe}_3\text{O}_4/20$  nm  $\text{Cr}_2\text{O}_3$  interface and  $\sim 3$  nm for the  $\text{Fe}_3\text{O}_4/5$  nm  $\text{Cr}_2\text{O}_3$  interface. In contrast, no significant differences in the extent of cation intermixing at the two interfaces are observed after irradiation. For both heterostructures, the interfacial width for both Cr and Fe increases to  $\sim 4 \pm 0.5$  nm. The increase in interfacial width after irradiation is qualitatively consistent with and the same order of magnitude as the width determined from STEM-EELS line profiles shown in Fig. 5. Although the intermixing appears in Fig. 7 to be biased toward Cr diffusion into  $\text{Fe}_3\text{O}_4$ , with less Fe diffusion into  $\text{Cr}_2\text{O}_3$ , this conclusion cannot be definitively drawn from comparison of the APT composition profiles. As described in the Supplemental Material [35], scaling challenges in the APT data at the heterointerface due to differences

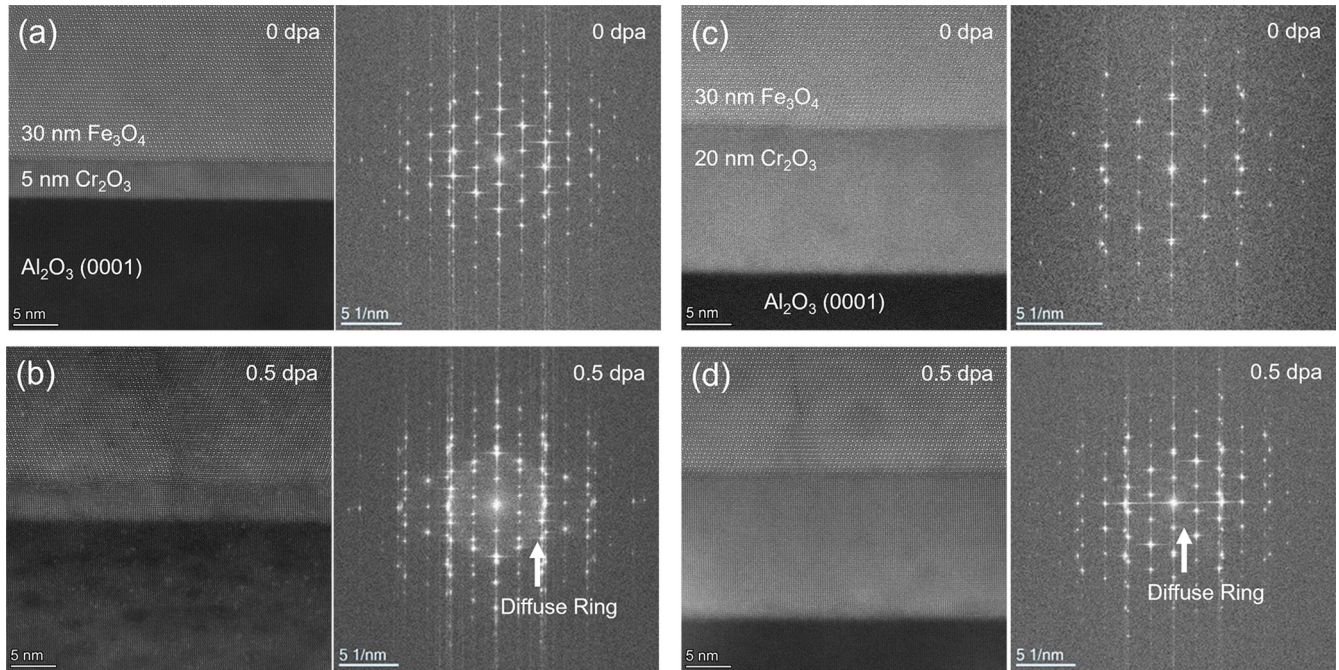


FIG. 4. Cross-sectional scanning transmission electron microscopy (STEM)-high-angle annular dark field (HAADF) images (right) and fast Fourier transforms (FFTs) of the entire stack (left) of as-grown  $\text{Fe}_3\text{O}_4/\text{Cr}_2\text{O}_3$  heterostructures and the same heterostructures after irradiation to 0.5 dpa, with (a) and (b) 5 nm and (c) and (d) 20 nm  $\text{Cr}_2\text{O}_3$  layers. Arrows indicate the presence of a diffuse ring in the FFT after irradiation.

in field evaporation of  $\text{Cr}_2\text{O}_3$  compared with  $\text{Fe}_3\text{O}_4$  make it impossible to place the as-grown and irradiated datasets on an absolute scale such that the exact distances can be compared between samples. Therefore, we cannot definitively establish the location of the original  $\text{Fe}_3\text{O}_4/\text{Cr}_2\text{O}_3$  interface in

either irradiated dataset. These scaling challenges are likely also responsible for the apparent increase in quantitative interface widths measured by APT (Fig. 7) compared with STEM-EELS (Fig. 5).

#### IV. DISCUSSION

Ion irradiation in vacuum has been shown previously to reduce  $\text{Fe}_3\text{O}_4$  to crystalline wüstite,  $\text{Fe}_{1-x}\text{O}$ , at high dose due to oxygen transport from  $\text{Fe}_3\text{O}_4$  to nearby metallic Fe [26]. As shown in the spatially resolved STEM-EELS spectra in Fig. 6, in this paper, we have captured the initial stages of  $\text{Fe}_3\text{O}_4$  reduction in which the fraction of  $\text{Fe}^{2+}$  increases relative to  $\text{Fe}^{3+}$  in the magnetite crystal structure. Both the Fe valence reduction measured by EELS and lattice disorder observed by RBS channeling (Fig. 2) are localized near the  $\text{Cr}_2\text{O}_3$  interface, indicating increased radiation damage accumulation at the interface compared with the film bulk or surface. This reduction of  $\text{Fe}_3\text{O}_4$  is consistent with both the generation of oxygen vacancies in the lattice and the formation of a  $(\text{Fe}, \text{Cr})_3\text{O}_4$  spinel due to radiation-induced cation intermixing in the interfacial region. In  $(\text{Fe}, \text{Cr})_3\text{O}_4$  spinels,  $\text{Cr}^{3+}$  substitutes for  $\text{Fe}^{3+}$  in octahedral sites of the spinel lattice [47]. We cannot determine to what extent the intermixing of  $\text{Cr}^{3+}$  is a driving force for the reduction of Fe in  $\text{Fe}_3\text{O}_4$  vs the radiation-induced generation of oxygen vacancies in the spinel lattice.

A comparison of the EELS spectra for  $\text{Fe}_3\text{O}_4$  on 5 nm  $\text{Cr}_2\text{O}_3$  and 20 nm  $\text{Cr}_2\text{O}_3$  at a dose of 0.5 dpa reveals more reduction in the film deposited on the thinner  $\text{Cr}_2\text{O}_3$  buffer layer [Figs. 6(c) and 6(d)]. Likewise, the lattice disorder at the  $\text{Fe}_3\text{O}_4/5$  nm  $\text{Cr}_2\text{O}_3$  interface increases more quickly

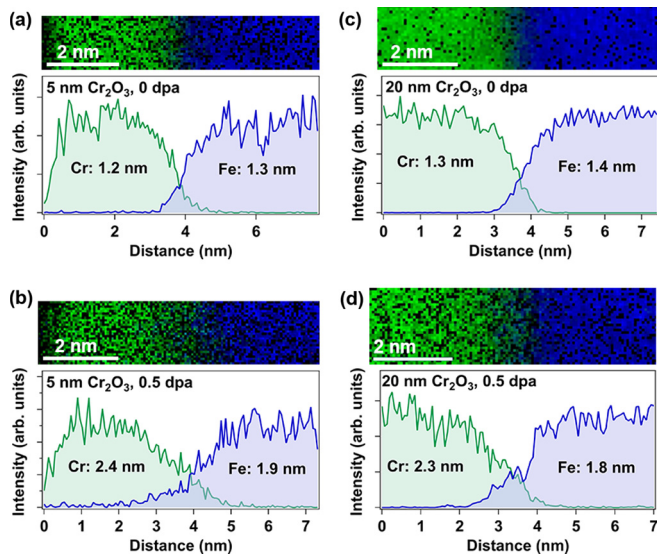


FIG. 5. Scanning transmission electron microscopy (STEM)-electron energy loss spectroscopy (EELS) maps (top) and integrated line profiles (bottom) of the Cr (green) and Fe (blue)  $L$  edges at the  $\text{Fe}_3\text{O}_4/\text{Cr}_2\text{O}_3$  interface for the films with (a) and (b) 5 nm  $\text{Cr}_2\text{O}_3$  and (c) and (d) 20 nm  $\text{Cr}_2\text{O}_3$ . Profiles are taken from (a) and (c) unirradiated films and (b) and (d) after irradiation to 0.5 dpa. Interfacial widths are indicated for both Cr and Fe in each figure.

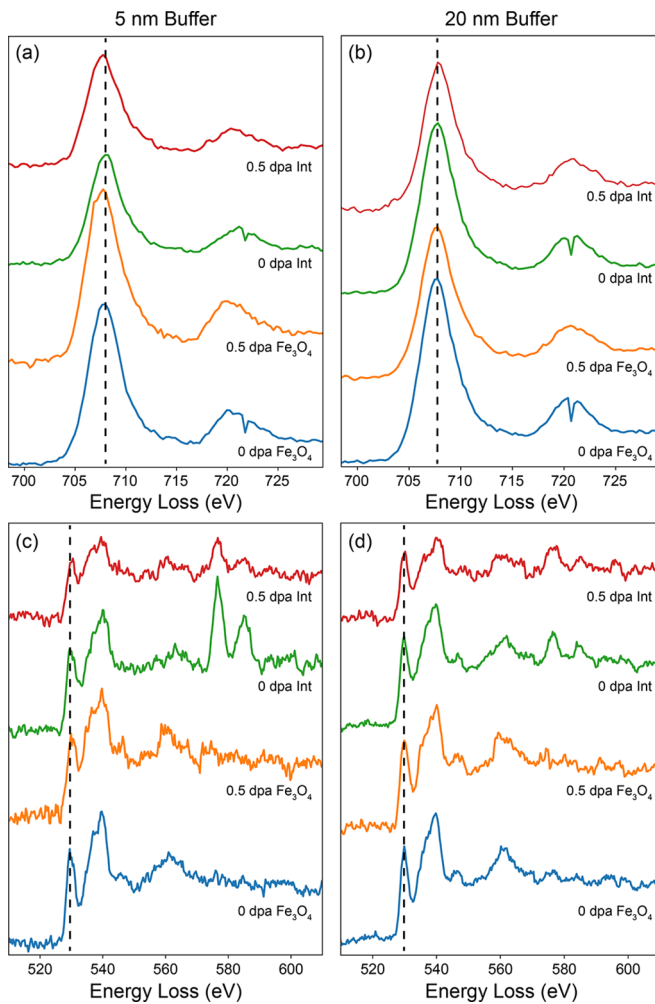


FIG. 6. Scanning transmission electron microscopy (STEM)-electron energy loss spectroscopy (EELS) spectra at the Fe  $L$  edge and O  $K$  edge, respectively, for the  $\text{Fe}_3\text{O}_4/\text{Cr}_2\text{O}_3$  heterostructure with (a) and (c) 5 nm and (b) and (d) 20 nm  $\text{Cr}_2\text{O}_3$ . Layer-resolved spectra were collected at the  $\text{Fe}_3\text{O}_4/\text{Cr}_2\text{O}_3$  interface (Int.) and in the  $\text{Fe}_3\text{O}_4$  film 3–4-unit cells away from the interface ( $\text{Fe}_3\text{O}_4$ ), for both the as-grown heterostructure (0 dpa) and after irradiation to 0.5 dpa. Vertical dashed lines in are guides to the eye of the Fe  $L_3$  and O  $K$  prepeak positions. The lower-intensity data point at  $\sim 721$  eV in some spectra is an artifact of the detector.

with dose than does the disorder at the  $\text{Fe}_3\text{O}_4/20$  nm  $\text{Cr}_2\text{O}_3$  interface [Fig. 2(c)], correlated with a larger extent of Cr intermixing into  $\text{Fe}_3\text{O}_4$  at the  $\text{Fe}_3\text{O}_4/5$  nm  $\text{Cr}_2\text{O}_3$  interface [Fig. 7(c)]. High-resolution STEM imaging of the two  $\text{Fe}_3\text{O}_4$  films before irradiation confirms that more misfit dislocations are present in the  $\text{Fe}_3\text{O}_4$  film deposited on pseudomorphically strained 5 nm  $\text{Cr}_2\text{O}_3$  [Fig. 3(b)], as expected from the larger lattice mismatch in this system. The role of misfit dislocations as a sink or antisink for radiation-induced point defects is complex [21], but in the case of  $\text{Fe}_3\text{O}_4$  on  $\text{Cr}_2\text{O}_3$ , it appears that the presence of structural defects such as misfit dislocations at the interface increases the accumulation of disorder at the interface of  $\text{Fe}_3\text{O}_4$ , at least under these conditions. We have shown previously that the nature of the misfit dislocations matters and that their simple presence is not enough to enhance defect annihilation [21]. This result confirms that

key finding in another context, highlighting the generality of this behavior and suggesting that the irradiation response of heterophase materials can be modified by controlling the nature of the interface.

Lastly, we note that the  $\text{Cr}_2\text{O}_3$  buffer layers exhibited significantly different backscattering channeling behavior than that observed for the  $\text{Fe}_3\text{O}_4$  overlayers. The minimum yield of the as-grown buffer layers of both thicknesses (5 and 20 nm) was considerably larger than that of the  $\text{Fe}_3\text{O}_4$  overlayers [Figs. 2(a) and 2(b)]. These higher yields are not attributed to dechanneling through the  $\text{Fe}_3\text{O}_4$  overlayers because of the low minimum yields in these overlayers but instead are reflective of a combination of disorder in the  $\text{Cr}_2\text{O}_3$  layers and dechanneling that may occur at misfit dislocations at the  $\text{Fe}_3\text{O}_4/\text{Cr}_2\text{O}_3$  interface. After irradiation to 0.5 dpa, the 5-nm-thick  $\text{Cr}_2\text{O}_3$  buffer layer exhibits a significant increase in channeling yield, reaching a value equivalent to the random yield. This behavior is often interpreted as full amorphization of the film. However, complementary STEM imaging of the irradiated heterostructure reveals that clear crystalline order is retained in the 5-nm-thick  $\text{Cr}_2\text{O}_3$  buffer layer after irradiation [Fig. 4(b)]. A high channeling minimum yield in conjunction with crystalline order suggests that irradiation of  $\text{Cr}_2\text{O}_3$  has produced a significant population of interstitials that occupy the channels in the crystalline lattice; interstitials are not easily visible by STEM imaging. The production of Cr interstitials during irradiation may also have contributed to the intermixing observed at the  $\text{Fe}_3\text{O}_4/\text{Cr}_2\text{O}_3$  interface after irradiation. Cr interstitials have been predicted to encounter smaller diffusion barriers along the  $c$  direction of the corundum lattice compared with the perpendicular direction [48], facilitating transport of Cr interstitials to the  $\text{Fe}_3\text{O}_4$  interface. Cation diffusion in  $\text{Fe}_3\text{O}_4$  is relatively fast [49], even in the absence of irradiation, enabling intermixing. As discussed above, this intermixing is further enabled by the presence of defects (misfit dislocations, oxygen vacancies) in  $\text{Fe}_3\text{O}_4$ .

## V. SUMMARY

The disordering response of epitaxial  $\text{Fe}_3\text{O}_4(111)$  thin films was studied before and after 400 keV  $\text{Ar}^{2+}$  irradiation to 0.1 and 0.5 dpa. The misfit dislocation density in the  $\text{Fe}_3\text{O}_4$  films was varied by controlling the thickness of the underlying  $\text{Cr}_2\text{O}_3(0001)$  epitaxial buffer layer to be below (5 nm) and above (20 nm) the critical thickness for epitaxial strain relaxation on  $\text{Al}_2\text{O}_3(0001)$ . STEM-HAADF imaging and Bragg-filtering analysis confirmed a higher misfit dislocation density in the  $\text{Fe}_3\text{O}_4/5$  nm  $\text{Cr}_2\text{O}_3$  heterostructure compared with the  $\text{Fe}_3\text{O}_4/20$  nm  $\text{Cr}_2\text{O}_3$  heterostructure, as expected from the larger lattice mismatch in the former case. After irradiation, both structures exhibited increased disorder in both the  $\text{Fe}_3\text{O}_4$  and  $\text{Cr}_2\text{O}_3$  layers, but the highest damage accumulation was observed in the  $\text{Cr}_2\text{O}_3$  buffer layer. On the  $\text{Fe}_3\text{O}_4$  side of the interface, damage accumulation, Fe valence reduction, and Cr intermixing into  $\text{Fe}_3\text{O}_4$  were all observed to occur to a greater extent in the  $\text{Fe}_3\text{O}_4$  film with the higher misfit dislocation density ( $\text{Fe}_3\text{O}_4/5$  nm  $\text{Cr}_2\text{O}_3$  heterostructure). This result indicates that misfit dislocations at the interface do not act as defect recombination



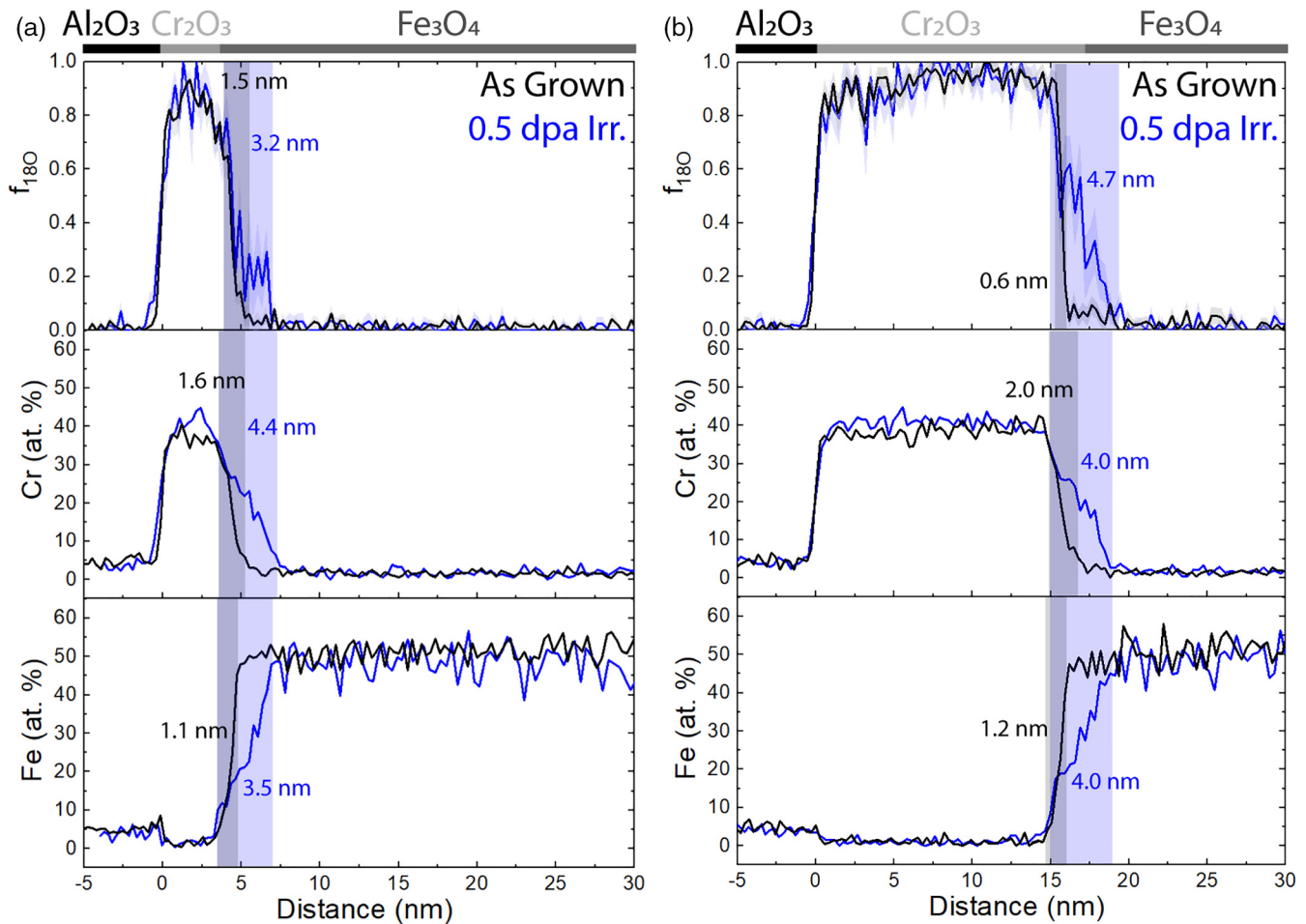


FIG. 7. One-dimensional (1D) fractional isotopic and composition profiles of  $^{18}\text{O}$ , Cr, and Fe taken from atom probe tomography (APT) reconstructions of as-grown and irradiated  $\text{Fe}_3\text{O}_4/\text{Cr}_2^{18}\text{O}_3$  heterostructures with (a) 5 nm and (b) 20 nm  $\text{Cr}_2\text{O}_3$  buffer layers. Profiles are aligned to the  $\text{Al}_2\text{O}_3/\text{Cr}_2\text{O}_3$  interface at a distance of 0 nm, with distance increasing to the film surface. Dark vertical shading and values indicate the intermixing region (90–10% of full intensity) in the as-grown heterostructure, and light shading and values indicate the intermixing region after irradiation. Statistical counting error is shown as shading around data (error is too small for shading to be observed in Cr and Fe profiles).

centers and instead increase the accumulation of damage at the interface of  $\text{Fe}_3\text{O}_4$ . The significant damage accumulation in the  $\text{Cr}_2\text{O}_3$  buffer layers observed by RBS channeling but not confirmed by STEM-HAADF images that indicated that the crystal structure was intact suggest the formation of Cr interstitials under irradiation. A large population of Cr interstitials may have contributed to the intermixing observed at the  $\text{Fe}_3\text{O}_4/\text{Cr}_2\text{O}_3$  interface.

**ACKNOWLEDGMENTS**

This paper was supported as part of Fundamental Understanding of Transport Under Reactor Extremes, an Energy Frontier Research Center funded by the U.S. Department of Energy (DOE), Office of Science, Basic Energy Sciences. C.O. acknowledges support from the DOE Early Career Research Program. Work at the Molecular Foundry was supported by the U.S. DOE, Office of Science, Basic Energy

Sciences under Contract No. DE-AC02-05CH11231. Y.W. acknowledges George Burns and Bill Wampler of Sandia Ion Beam Lab for their help with RBS measurements. Ion beam irradiation and RBS measurements were performed at the Center for Integrated Nanotechnologies (CINT) jointly operated by Los Alamos and Sandia National Laboratories for DOE Office of Science. Los Alamos National Laboratory, an affirmative action/equal opportunity employer, is managed by Triad National Security, LLC, for the U.S. DOE’s NNSA, under Contract No. 89233218CNA000001. Sample preparation and APT measurements were performed on a project award (No. 10.46936/cpcy.proj.2022.60581/60008638) from the Environmental Molecular Sciences Laboratory, a national scientific user facility sponsored by the U.S. DOE’s Office of Biological and Environmental Research and located at Pacific Northwest National Laboratory (PNNL). PNNL is a multi-program national laboratory operated by Battelle for the U.S. DOE under Contract No. DE-AC05-79RL01830.

- [1] K. Nordlund, S. J. Zinkle, A. E. Sand, F. Granberg, R. S. Averback, R. E. Stoller, T. Suzudo, L. Malerba, F. Banhart, W. J. Weber *et al.*, Primary radiation damage: A review of current understanding and models, *J. Nucl. Mater.* **512**, 450 (2018).
- [2] A. J. Ardell and P. Bellon, Radiation-induced solute segregation in metallic alloys, *Curr. Opin. Solid State Mat. Sci.* **20**, 115 (2016).
- [3] W. J. Weber, R. C. Ewing, C. R. A. Catlow, T. D. de la Rubia, L. W. Hobbs, C. Kinoshita, H. Matzke, A. T. Motta, M. Nastasi, E. K. H. Salje *et al.*, Radiation effects in crystalline ceramics for the immobilization of high-level nuclear waste and plutonium, *J. Mater. Res.* **13**, 1434 (1998).
- [4] N. Itoh and K. Tanimura, Radiation effects in ionic solids, *Radiat. Eff. Defect. S.* **98**, 269 (1986).
- [5] S. J. Zinkle, V. A. Skuratov, and D. T. Hoelzer, On the conflicting roles of ionizing radiation in ceramics, *Nucl. Instrum. Meth. B* **191**, 758 (2002).
- [6] Y. W. Zhang and W. J. Weber, Ion irradiation and modification: The role of coupled electronic and nuclear energy dissipation and subsequent nonequilibrium processes in materials, *Appl. Phys. Rev.* **7**, 041307 (2020).
- [7] I. J. Beyerlein, A. Caro, M. J. Demkowicz, N. A. Mara, A. Misra, and B. P. Uberuaga, Radiation damage tolerant nanomaterials, *Mater. Today* **16**, 443 (2013).
- [8] X. H. Zhang, K. Hattar, Y. X. Chen, L. Shao, J. Li, C. Sun, K. Y. Yu, N. Li, M. L. Taheri, H. Y. Wang *et al.*, Radiation damage in nanostructured materials, *Prog. Mater. Sci.* **96**, 217 (2018).
- [9] T. C. Kaspar, J. G. Gigax, L. Shao, M. E. Bowden, T. Varga, V. Shutthanandan, S. R. Spurgeon, P. F. Yan, C. M. Wang, P. Ramuhalli *et al.*, Damage evolution of ion irradiated defected-fluorite  $\text{La}_2\text{Zr}_2\text{O}_7$  epitaxial thin films, *Acta Mater.* **130**, 111 (2017).
- [10] S. R. Spurgeon, Order-disorder behavior at thin film oxide interfaces, *Curr. Opin. Solid State Mat. Sci.* **24**, 100870 (2020).
- [11] S. R. Spurgeon, T. C. Kaspar, V. Shutthanandan, J. Gigax, L. Shao, and M. Sassi, Asymmetric lattice disorder induced at oxide interfaces, *Adv. Mater. Interfaces* **7**, 1901944 (2020).
- [12] P. P. Dholabhai, G. Pilania, J. A. Aguiar, A. Misra, and B. P. Uberuaga, Termination chemistry-driven dislocation structure at  $\text{SrTiO}_3/\text{MgO}$  heterointerfaces, *Nat. Commun.* **5**, 5043 (2014).
- [13] J. A. Aguiar, P. P. Dholabhai, Z. X. Bi, Q. X. Jia, E. G. Fu, Y. Q. Wang, T. Aoki, J. T. Zhu, A. Misra, and B. P. Uberuaga, Linking interfacial step structure and chemistry with locally enhanced radiation-induced amorphization at oxide heterointerfaces, *Adv. Mater. Interfaces* **1**, 1300142 (2014).
- [14] M. Sassi, T. Kaspar, K. M. Rosso, and S. R. Spurgeon, Effect of structure and composition on the electronic excitation induced amorphization of  $\text{La}_2\text{Ti}_{2-x}\text{Zr}_x\text{O}_7$  ceramics, *Sci. Rep.* **9**, 8190 (2019).
- [15] B. K. Derby, Y. Sharma, J. A. Valdez, M. Chancey, Y. Q. Wang, E. L. Brosha, D. J. Williams, M. M. Schneider, A. Chen, B. P. Uberuaga *et al.*, Interfacial cation mixing and microstructural changes in bilayer GTO/GZO thin films after irradiation, *JOM* **74**, 4015 (2022).
- [16] Z. X. Bi, B. P. Uberuaga, L. J. Vernon, J. A. Aguiar, E. G. Fu, S. J. Zheng, S. X. Zhang, Y. Q. Wang, A. Misra, and Q. X. Jia, Role of the interface on radiation damage in the  $\text{SrTiO}_3/\text{LaAlO}_3$  heterostructure under  $\text{Ne}^{2+}$  ion irradiation, *J. Appl. Phys.* **115**, 124315 (2014).
- [17] Z. Bi, B. P. Uberuaga, L. J. Vernon, E. Fu, Y. Wang, N. Li, H. Wang, A. Misra, and Q. X. Jia, Radiation damage in heteroepitaxial  $\text{BaTiO}_3$  thin films on  $\text{SrTiO}_3$  under Ne ion irradiation, *J. Appl. Phys.* **113**, 023513 (2013).
- [18] M. J. Zhuo, E. G. Fu, L. Yan, Y. Q. Wang, Y. Y. Zhang, R. M. Dickerson, B. P. Uberuaga, A. Misra, M. Nastasi, and Q. X. Jia, Interface-enhanced defect absorption between epitaxial anatase  $\text{TiO}_2$  film and single crystal  $\text{SrTiO}_3$ , *Scr. Mater.* **65**, 807 (2011).
- [19] M. J. Zhuo, B. P. Uberuaga, L. Yan, E. G. Fu, R. M. Dickerson, Y. Q. Wang, A. Misra, M. Nastasi, and Q. X. Jia, Radiation damage at the coherent anatase  $\text{TiO}_2/\text{SrTiO}_3$  interface under Ne ion irradiation, *J. Nucl. Mater.* **429**, 177 (2012).
- [20] B. E. Matthews, M. Sassi, C. Barr, C. Ophus, T. C. Kaspar, W. L. Jiang, K. Hattar, and S. R. Spurgeon, Percolation of ion-irradiation-induced disorder in complex oxide interfaces, *Nano Lett.* **21**, 5353 (2021).
- [21] V. Shutthanandan, S. Choudhury, S. Manandhar, T. C. Kaspar, C. Wang, A. Devaraj, B. D. Wirth, S. Thevuthasan, R. G. Hoagland, P. P. Dholabhai *et al.*, Radiation tolerant interfaces: Influence of local stoichiometry at the misfit dislocation on radiation damage resistance of metal/oxide interfaces, *Adv. Mater. Interfaces* **4**, 1700037 (2017).
- [22] M. J. Demkowicz, P. Bellon, and B. D. Wirth, Atomic-scale design of radiation-tolerant nanocomposites, *MRS Bull.* **35**, 992 (2010).
- [23] S. J. Zinkle and J. T. Busby, Structural materials for fission & fusion energy, *Mater. Today* **12**, 12 (2009).
- [24] K. Kruska, S. Lozano-Perez, D. W. Saxey, T. Terachi, T. Yamada, and G. D. W. Smith, Nanoscale characterisation of grain boundary oxidation in cold-worked stainless steels, *Corrosion Sci.* **63**, 225 (2012).
- [25] A. Devaraj, D. J. Barton, C. H. Li, S. V. Lambeets, T. K. Liu, A. Battu, S. Vaithiyalingam, S. Thevuthasan, F. P. Yang, J. H. Guo *et al.*, Visualizing the nanoscale oxygen and cation transport mechanisms during the early stages of oxidation of Fe-Cr-Ni alloy using *in situ* atom probe tomography, *Adv. Mater. Interfaces* **9**, 2200134 (2022).
- [26] W. L. Jiang, J. A. Sundararajan, T. Varga, M. E. Bowden, Y. Qiang, J. S. McCloy, C. H. Henager, and R. O. Montgomery, *In situ* study of nanostructure and electrical resistance of nanocluster films irradiated with ion beams, *Adv. Funct. Mater.* **24**, 6210 (2014).
- [27] M. Krupska, N. T. H. Kim-Ngan, A. G. Balogh, P. Malinsky, and A. Mackova, 1 MeV  $\text{Ar}^+$  and  $\text{Kr}^+$  ion irradiation induced intermixing in single- and bi-layer  $\text{Fe}_3\text{O}_4$  films grown on  $\text{MgO}(001)$  single crystals, *Surf. Coat. Tech.* **355**, 90 (2018).
- [28] M. Owusu-Mensah, J. Cooper, A. L. Morales, K. Yano, S. D. Taylor, D. K. Schreiber, B. P. Uberuaga, and D. Kaoumi, Surprisingly high irradiation-induced defect mobility in  $\text{Fe}_3\text{O}_4$  as revealed through *in situ* transmission electron microscopy, *Mater. Charact.* **187**, 111863 (2022).
- [29] T. C. Kaspar, P. Hatton, K. H. Yano, S. D. Taylor, S. R. Spurgeon, B. P. Uberuaga, and D. K. Schreiber, Adatom-driven oxygen intermixing during the deposition of oxide thin films by molecular beam epitaxy, *Nano Lett.* **22**, 4963 (2022).
- [30] J. F. Ziegler, The Stopping and Range of Ions in Matter (SRIM), 2013, <http://www.srim.org/>.
- [31] W.-K. Chu, J. W. Mayer, and M.-A. Nicolet, *Backscattering Spectrometry* (Academic Press, Inc., New York, 1978).

- [32] M. J. Hytch and L. Potez, Geometric phase analysis of high-resolution electron microscopy images of antiphase domains: Example  $\text{Cu}_3\text{Au}$ , *Philos. Mag. A* **76**, 1119 (1997).
- [33] K. Thompson, D. Lawrence, D. J. Larson, J. D. Olson, T. F. Kelly, and B. Gorman, *In situ* site-specific specimen preparation for atom probe tomography, *Ultramicroscopy* **107**, 131 (2007).
- [34] K. H. Yano, A. A. Kohnert, T. C. Kaspar, S. D. Taylor, S. R. Spurgeon, H. Kim, Y. Q. Wang, B. P. Uberuaga, and D. K. Schreiber, Radiation enhanced anion diffusion in chromia, *J. Phys. Chem. C* **125**, 27820 (2021).
- [35] See Supplemental Material at <http://link.aps.org/supplemental/10.1103/PhysRevMaterials.7.093604> for RHEED line spacing analysis, additional RBS spectra, additional STEM data, and additional details of the APT analysis.
- [36] T. C. Kaspar, S. E. Chamberlin, and S. A. Chambers, Surface structure of  $\alpha\text{-Cr}_2\text{O}_3(0001)$  after activated oxygen exposure, *Surf. Sci.* **618**, 159 (2013).
- [37] S. A. Chambers, Y. Liang, and Y. Gao, Noncommutative band offset at  $\alpha\text{-Cr}_2\text{O}_3/\alpha\text{-Fe}_2\text{O}_3(0001)$  heterojunctions, *Phys. Rev. B* **61**, 13223 (2000).
- [38] C. J. Goss, Saturation magnetization, coercivity and lattice-parameter changes in the system  $\text{Fe}_3\text{O}_4\text{-}\gamma\text{-Fe}_2\text{O}_3$ , and their relationship to structure, *Phys. Chem. Miner.* **16**, 164 (1988).
- [39] O. Meyer, F. Weschenfelder, X. X. Xi, G. C. Xiong, G. Linker, and J. Geerk, Channeling analysis of intrinsic and radiation-induced disorder in single crystalline high- $T_c$   $\text{YBa}_2\text{Cu}_3\text{O}_7$  thin films, *Nucl. Instrum. Meth. B* **35**, 292 (1988).
- [40] C. E. Carlton and P. J. Ferreira, *In situ* TEM nanoindentation of nanoparticles, *Micron* **43**, 1134 (2012).
- [41] M. W. Chu, I. Szafraniak, R. Scholz, C. Harnagea, D. Hesse, M. Alexe, and U. Gosele, Impact of misfit dislocations on the polarization instability of epitaxial nanostructured ferroelectric perovskites, *Nat. Mater.* **3**, 87 (2004).
- [42] Y. Y. Zhu, C. Y. Song, A. M. Minor, and H. Y. Wang, Cs-corrected scanning transmission electron microscopy investigation of dislocation core configurations at a  $\text{SrTiO}_3/\text{MgO}$  heterogeneous interface, *Microsc. Microanal.* **19**, 706 (2013).
- [43] L. J. Allen, S. D. Findlay, A. R. Lupini, M. P. Oxley, and S. J. Pennycook, Atomic-Resolution Electron Energy Loss Spectroscopy Imaging in Aberration Corrected Scanning Transmission Electron Microscopy, *Phys. Rev. Lett.* **91**, 105503 (2003).
- [44] C. Colliex, T. Manoubi, and C. Ortiz, Electron-energy-loss-spectroscopy near-edge fine-structures in the iron-oxygen system, *Phys. Rev. B* **44**, 11402 (1991).
- [45] J. Bischoff and A. T. Motta, EFTEM and EELS analysis of the oxide layer formed on HCM12A exposed to SCW, *J. Nucl. Mater.* **430**, 171 (2012).
- [46] M. Varela, M. P. Oxley, W. Luo, J. Tao, M. Watanabe, A. R. Lupini, S. T. Pantelides, and S. J. Pennycook, Atomic-resolution imaging of oxidation states in manganites, *Phys. Rev. B* **79**, 085117 (2009).
- [47] S. A. Chambers, T. C. Droubay, T. C. Kaspar, I. H. Nayyar, M. E. McBriarty, S. M. Heald, D. J. Keavney, M. E. Bowden, and P. V. Sushko, Electronic and optical properties of a semi-conducting spinel ( $\text{Fe}_2\text{CrO}_4$ ), *Adv. Funct. Mater.* **27**, 1605040 (2017).
- [48] A. Banerjee, A. A. Kohnert, E. F. Holby, and B. P. Uberuaga, Interplay between defect transport and cation spin frustration in corundum-structured oxides, *Phys. Rev. Mater.* **5**, 034410 (2021).
- [49] J. A. Van Orman and K. L. Crispin, in *Diffusion in Minerals and Melts*, edited by Y. X. Zhang and D. J. Cherniak (Mineralogical Society of America, Chantilly, 2010), Vol. 72, p. 757.